1   Revision 2: MS# 5742

2   **High-pressure compressibility and vibrational properties of (Ca,Mn)CO$_3$**

3   Jin Liu[1], Razvan Caracas[2], Dawei Fan[3], Ema Bobocioiu[2],

4   Dongzhou Zhang[4], Wendy L. Mao[1,5]

5   [1]Department of Geological Sciences, Stanford University, Stanford, CA 94305, USA

6   [2]CNRS, Laboratoire de Géologie de Lyon, Université Claude Bernard Lyon 1, 69342 Lyon

7   Cedex 07, France

8   [3]Key Laboratory of High-temperature and High-pressure Study of the Earth's Interior,

9   Institute of Geochemistry, Chinese Academy of Sciences, Guiyang, Guizhou 550002, China

10   [4]Hawai'i Institute of Geophysics and Planetology, University of Hawai'i at Manoa, Honolulu,

11   HI 96822, USA

12   [5]Stanford Institute for Materials and Energy Sciences, SLAC National Accelerator

13   Laboratory, Menlo Park, CA 94025, USA

14

15   **Abstract**

16   Knowledge of potential carbon carriers such as carbonates is critical for our understanding of

17   the deep-carbon cycle and related geological processes within the planet. Here we

18   investigated the high-pressure behavior of (Ca,Mn)CO$_3$ up to 75 GPa by synchrotron single-

19   crystal X-ray diffraction, laser Raman spectroscopy, and theoretical calculations. MnCO$_3$-

20   rich carbonate underwent a structural phase transition from the CaCO$_3$-I structure into the

21   CaCO$_3$-VI structure at 45-48 GPa, while CaCO$_3$-rich carbonate transformed into CaCO$_3$-III

22   and CaCO$_3$-VI at approximately 2 and 15 GPa, respectively. The equation of state and

23   vibrational properties of MnCO$_3$-rich and CaCO$_3$-rich carbonates changed dramatically

24   across the phase transition. The $CaCO_3$-VI-structured $CaCO_3$-rich and $MnCO_3$-rich

25   carbonates were stable at room temperature up to at least 53 and 75 GPa, respectively. The

26   addition of smaller cations (e.g., Mn^{2+}, Mg^{2+}, and Fe^{2+}) can enlarge the stability field of the

27    $CaCO_3$-I phase as well as increase the pressure for the structural transition into the $CaCO_3$-VI

28   phase.

29   **Keywords:** Carbonate, X-ray diffraction, Raman spectroscopy, High pressure

30

1. Introduction

32   Carbonates are the major, oxidized carbon-bearing phases in the Earth's crust and represent

33   an important carrier of carbon back into the mantle. The high-pressure behavior of carbonates

34   is thus essential for understanding deep-carbon cycling and storage in the Earth's deep

35   interior (Dasgupta and Hirschmann, 2010; Hazen and Schiffries, 2013). All naturally-

36   occurring carbonates in the crust can be potentially subducted into the deep mantle at

37   subduction zones. In particular, $CaCO_3$ is the dominant carbonate phase in the Earth's crust

38   and has been extensively investigated in static and dynamic high-pressure studies (e.g., Liu

39   and Mernagh, 1990; Williams et al., 1992; Biellmann et al., 1993; Gillet et al., 1993; Fiquet

40   et al., 1994; Suito et al., 2001; Ono et al., 2005; Oganov et al., 2006; Ono et al., 2007;

41   Merlini et al., 2012b; Shi et al., 2012; Ishizawa et al., 2013). $CaCO_3$ adopts a rhombohedral

42   R-3c structure at ambient conditions (referred to as $CaCO_3$-I) and undergoes a series of

43   structural phase transitions upon compression at room temperature into $CaCO_3$-II, -III, and -

44   VI approximately at 1.7, 2-3, and 15 GPa, respectively (Suito et al., 2001; Catalli and

45   Williams, 2005; Merlini et al., 2012b). $CaCO_3$-I, -II, and -III transform into aragonite at

46   elevated temperatures and then become disordered calcite when approaching the liquidus

47   (Suito et al., 2001), while the phase stability of calcite-VI is not well constrained at high

48   pressure and temperature (*P-T*).

49

50   At ambient conditions, there is a continuous solid solution between $CaCO_3$ and $MnCO_3$.

51   $MnCO_3$ occurs in the $CaCO_3$-I structure at ambient conditions and its high-pressure behavior

52   has been the subject of debate. The dissociation of $MnCO_3$ was observed at 6-8 GPa and

53   2273 K (Liu et al., 2001), while $MnCO_3$ was argued to be stable up to ~47 GPa and 2000 K

54   (Santillan and Williams, 2004) and then to transform into an orthorhombic phase at 50 GPa

55   above 1500 K (Ono, 2007). Furthermore, a series of transitions in $MnCO_3$ at room

56   temperature were observed at 15 and 50 GPa, respectively (Farfan et al., 2013). In the most

57   recent studies, $MnCO_3$ was observed to transform into the $CaCO_3$-VI structure at room

58   temperature upon compression, although those studies reported a different phase transition

59   pressure of either ~35 GPa (Boulard et al., 2015) or 44 GPa (Merlini et al., 2015). Hereafter

60   the low-pressure ($CaCO_3$-I) and high-pressure ($CaCO_3$-VI) phases of $MnCO_3$ will be referred

61   to as $MnCO_3$-I and $MnCO_3$-II, respectively, after Merlini et al. (2015). Furthermore, the

62   compressibility and vibrational properties of $MnCO_3$-II have not been determined. Here we

63   combine synchrotron single-crystal X-ray diffraction (XRD) and laser Raman spectroscopy,

64   together with theoretical calculations to study the high-pressure behavior of $(Ca,Mn)CO_3$ up

65   to 75 GPa.

66

67   **2. Methods**

68   Natural calcite and rhodochrosite starting samples were obtained from Dabie Mountain,

69   China. Based on electron microprobe analyses, the composition of calcite was determined to

70   be $(Ca_{0.992}Mn_{0.008})CO_3$ with very minor amounts less than 0.1% of Mg and Fe, while the

71   rhodochrosite sample was $(Ca_{0.009}Mn_{0.980}Fe_{0.009}Mg_{0.002})CO_3$. For simplicity, we will herein

72   refer to these two samples as $CaCO_3$ and $MnCO_3$, respectively. Both $CaCO_3$ and $MnCO_3$

73   starting samples exhibit a rhombohedral shape, reflecting their R-$3c$ structure.

74

75   **2.1. Single-crystal X-ray diffraction**

76   Single-crystal XRD analyses confirmed the $CaCO_3$-I structure of the $MnCO_3$ starting sample

77   with lattice parameters a = 4.7762(15) Å and c = 15.6477(68) Å at ambient conditions. A

78   small platelet of single-crystal $MnCO_3$ of ~5 μm thick and ~40 μm in diameter was loaded

79   into a symmetric diamond anvil cell (DAC). A tungsten (W) gasket was pre-indented by a

80   pair of diamond anvils having 300 μm flat culets to a thickness of ~30 μm. A hole of 170 μm

81   in diameter was drilled in the pre-indented gasket and used as a sample chamber. A small

82   piece of Pt foil was for use as a pressure calibrant. The pressure-transmitting medium, Ne,

83   was loaded into the sample chamber at GSECARS of the Advanced Photon Source (APS),

84   Argonne National Laboratory (ANL). High-pressure single-crystal XRD experiments were

85   conducted at beamline 13-IDD of the APS, ANL, using a monochromatic X-ray beam with a

86   wavelength of 0.3344 Å which was focused down to ~5 μm in diameter at the sample

87   position. XRD patterns were recorded on a MarCCD detector where the DAC was rotated

88   from -15° to + 15° about the X-ray beam direction with an interval of one degree. The tilting

89   and rotation of the MarCCD detector relative to the incident X-ray beam were calibrated

90   using lanthanum hexaboride (LaB_6) powder as the X-ray diffraction standard. The calibrated

91   distance between sample and MarCCD detector was 196.79 mm. XRD images were

92   processed and integrated using the Fit2D software for deriving the lattice parameters of the

93   pressure calibrant polycrystalline Pt (Hammersley et al. 1996). The same piece of sample

94   was used for ambient and high-pressure experiments. The different phases and lattice

95   parameters of MnCO$_3$ were extracted by the GSE_ADA/RSV software packages (Table S1)

96   (Dera et al., 2013). Pressure was calculated from the Pt pressure calibrant using a third-order

97   Birch-Murnaghan equation of state (3rd BM EoS) (Fei et al., 2007).

98

99   **2.2. Laser Raman spectroscopy**

100   High-pressure laser Raman spectra of CaCO$_3$ and MnCO$_3$ were collected using a Renishaw

101   RM1000 Raman microscope equipped with a 250 mm spectrometer focal length in the

102   Extreme Environments Laboratory (EEL) at Stanford University. The Raman system uses a

103   514.5 nm laser excitation line and has a spectral resolution of 4 cm^{-1} with the holographic

104   diffraction grating of 1800 lines/mm. The laser with a maximum power of 25 mW was

105   focused through a Nikon L Plan EPI 20X, 0.35 objective onto the sample with the laser spot

106   of approximately 2 μm in diameter. The Raman spectra were collected between -450 to

107   +1600 cm^{-1}. The single-crystal samples of ~10 μm thick and ~40 μm in diameter were loaded

108   into the sample chamber of a DAC with the (101) crystal plane facing the incident laser beam,

109   together with a few ruby spheres as the pressure calibrant (Mao et al., 1986). Helium was

110   loaded into the sample chamber as the pressure-transmitting medium using the high-pressure

111   gas loading system in the EEL. Pressure and uncertainties were determined by averaging

112   over multiple measurements of ruby spheres before and after each Raman spectrum. We note

113   that the Raman spectra of the sample for XRD experiments were measured during

114   decompression, indicating that the high-pressure phase transition of MnCO$_3$ was reversible.

115   Raman spectra were processed using the software PeakFit v4.12 with the Voigt area method.

116

117 **2.3. Theoretical Methods**

118 Theoretical Raman spectra were computed at 0 K using the density-functional perturbation

119 theory (Baroni and Resta, 1986; Baroni et al., 2001; Gonze et al., 2005) in the ABINIT

120 implementation (Veithen et al., 2005; Gonze et al., 2009) with planewaves and

121 pseudopotentials. We used experimental input for the starting configurations of the crystal

122 structures for $CaCO_3$-I (Graf, 1961), $CaCO_3$-III (Pippinger et al., 2015) and $CaCO_3$-VI

123 (Merlini et al., 2012b). We used Troullier-Martins-type pseudopotentials to describe the core

124 electrons (Fuchs and Scheffler, 1999). We employed 12 electronic bands per $CaCO_3$ formula

125 unit. The first Brillouin zone of the reciprocal space was sampled using 8x8x8, 4x4x4 and

126 6x6x6 regular grids of **k**-points (Monkhorst and Pack, 1976) for respectively the three

127 structures. Together with a kinetic energy cutoff of 40 Ha (1Ha = 27.2116 eV) this converged

128 the energy at better than 1 mHa per unit cell. The structures were first relaxed at the target

129 pressure, i.e., the atoms are displaced and the unit cell shape and volume are allowed to

130 change under symmetry constraints until the forces are minimized and the stresses have only

131 hydrostatic components. The Raman spectra were calculated on the relaxed structures: the

132 position of the peaks comes from the quasi-harmonic approximation, and the reported

133 intensity of the peaks is the average of the Raman tensors over all possible crystal

134 orientations and laser polarizations, as for ideal powders. More details can be found in the

135 WURM project original reference (Caracas and Bobocioiu, 2011) and website

136 (http://wurm.info), including the spectra and the corresponding atomic displacement patterns.

137

138 **3. Results and Discussion**

139   We conducted two experimental runs and obtained the single-crystal XRD patterns for

140   MnCO$_3$ up to 67 GPa at 300 K. The XRD patterns demonstrated that the rhombohedral

141   MnCO$_3$-I was stable up to 45 GPa at ambient temperature (Figs. 1-2). At higher pressures,

142   the XRD patterns of MnCO$_3$ changed (Fig. 1 inserts). The X-ray diffraction spots of MnCO$_3$

143   at 48-67 GPa could be well indexed to the crystal structure of CaCO$_3$-VI (Merlini et al.,

144   2012a). Laser Raman spectra of CaCO$_3$ and MnCO$_3$ were collected with pressure steps of 1–

145   3 GPa up to 53 and 75 GPa, respectively (Figs. 3-4). Raman spectra for CaCO$_3$ changed

146   around 2 and 15 GPa, respectively, while those for MnCO$_3$ started changes around 44 and 46

147   GPa. For CaCO$_3$, Raman spectra were assigned to CaCO$_3$-I below 1.9 GPa, to CaCO$_3$-III

148   between 1.9-15 GPa, and to CaCO$_3$-VI above 15 GPa, respectively. For MnCO$_3$, Raman

149   spectra were assigned to MnCO$_3$-I below 44 GPa, and to MnCO$_3$-II above 47 GPa, and to a

150   mixture of these two in between. Vibrational modes of CaCO$_3$ in the CaCO$_3$-I, -III, and -VI

151   structure were theoretically calculated in order to better understand the observed Raman

152   bands at high pressures (Figs. 5-6; see Tables S2-S4 in Supplementary Materials for more

153   details).

154

155   **3.1. Equation of state and compressibility of MnCO$_3$**

156   The pressure-volume (*P-V*) curve between 0 and 44 GPa was fit to a 3rd BM EoS to derive

157   the elastic parameters of MnCO$_3$-I, yielding the zero bulk modulus K_0 = 122(3) GPa and the

158   pressure derivative of bulk modulus $K' = 3.7(2)$, or K_0 = 113(3) GPa if K' was fixed at 4,

159   with the zero unit-cell volume V_0 = 309.1(1) Å^3 from XRD measurements at ambient

160   conditions (Tale S1). The derived EoS parameters in this study are comparable to most

161   previous studies (Zhang and Reeder, 1999; Boulard et al., 2015; Merlini et al., 2015), but

162   slightly lower than those of $MnCO_3$ reported by Ono (2007). The discrepancy may be due to

163   the lack of a pressure medium and fewer data points in the study by Ono (2007).

164

165   The relative axial compressibilities, a/a_0 and c/c_0, and the axial ratio, c/a, of $MnCO_3$-I were

166   determined as a function of pressure up to 44 GPa (Fig. 2). The compressibility of $MnCO_3$-I

167   is not isotropic, with the a axis about 3–4 times less compressible than the c axis which is

168   consistent with the results reported by Boulard et al. (2015). The anisotropic change in the a

169   and c axes causes the octahedral distortion to change from trigonally elongated to trigonally

170   compressed with increasing pressure (Lavina et al., 2010). The $(Mg,Fe)CO_3$ solid-solution

171   series exhibits a similar anisotropic behavior in the a/a_0 and c/c_0 ratios at high pressures

172   (Lavina et al., 2010). The a/a_0 and c/c_0 values were approximately 0.96 and 0.86,

173   respectively, for $MgCO_3$, $FeCO_3$, and $MnCO_3$ at ~40 GPa (e.g., Zhang et al., 1998; Fiquet et

174   al., 2002; Litasov et al., 2008; Lavina et al., 2010; Lin et al., 2012). The comparable axis

175   compressibilities of $MgCO_3$, $FeCO_3$, and $MnCO_3$ are likely due to them having the same

176   structure.

177

178     $MnCO_3$-I started to transform into $MnCO_3$-II at 45 GPa and the phase transition was

179   completed at 48 GPa. A complex diffraction pattern was observed at 47 GPa (Fig. 1 insert),

180   which cannot be indexed solely by $MnCO_3$-I or $MnCO_3$-II. This pattern contained both

181   phases, indicating that $MnCO_3$-I and $MnCO_3$-II could coexist prior to the completion of

182   phase transition. The observed transition pressure of $MnCO_3$ in this study is a few GPa

183   higher than that of $(Mn_{0.96}Ca_{0.04})CO_3$ reported by Merlini et al. (2015), indicating that a small

184   amount of Ca^{2+} might effectively reduce the transition pressure in the $(Ca,Mn)CO_3$ solid-

185   solution system. We note that Farfan et al. (2013) and Boulard et al. (2015) reported a

186   transition of $MnCO_3$ between 15 and 35 GPa using NaCl or silicon oil as the pressure-

187   transmitting medium and that this transition is not consistent with the $CaCO_3$-II and -VI

188   structures and may be related to a distortion of the $CaCO_3$-I structure due to nonhydrostatic

189   conditions, especially when NaCl undergoes a B1 to B2 phase transition about 25-30 GPa,

190   which involves a fairly large volume change. In contrast, both Merlini et al. (2015) and this

191   study used Ne and/or He as a pressure-transmitting medium in the single-crystal XRD

192   measurements and did not observe the distorted phase of the $CaCO_3$-I structure between 15

193   and 30 GPa. Similarly, Ono (2007) did not observe this distorted phase likely because the

194    $MnCO_3$ sample was annealed to 1000-1500 K to relax any differential stress at high pressures.

195   In particular, Merlini et al. (2015) observed $MnCO_3$ in the $CaCO_3$-VI structure at ~36 GPa

196   during decompression, while Boulard et al. (2015) observed the presence of diffraction peaks

197   other than from $MnCO_3$-I above ~35 GPa in the power XRD patterns using NaCl as the

198   pressure-transmitting medium. To date, the transition pressure of $MnCO_3$ into the $CaCO_3$-VI

199   structure has been reported ranging approximately from 35 to 50 GPa, which seems sensitive

200   to the stress field in the sample chambers. In addition, Santillan and Williams (2004) did not

201   observe any phase transition up to 50 GPa, likely because the incorporation of 16 mol% of

202   Fe^{2+} and Mg^{2+} in their $MnCO_3$ sample could greatly enlarge the stability field of the calcite

203   structure of $MnCO_3$. The addition of Fe and Mg into $MnCO_3$ could thus greatly enlarge the

204   stability field of calcite structured $MnCO_3$. This is similar to the idea presented by Shi et al.

205   (2012) that an increase in Mn concentration in $CaCO_3$ expanded the high-pressure stability

206   range of the different $CaCO_3$ structures.

207

208   The P-V curve of MnCO$_3$-II was fit to a second-order BM EoS from 48 to 67 GPa, resulting

209   in $K_0 = 144(13)$ GPa and $V_0 = 285(7)$ Å^3 with K' fixed at 4. The unit cell volume per formula

210   (V/Z) of MnCO$_3$-II reported by Merlini et al. (2015) is close to the P-V curve extrapolated by

211   the current EoS of MnCO$_3$-II. The bulk modulus of MnCO$_3$ increases approximately by 12%

212   across the phase transition from I to II. The density of MnCO$_3$ showed a dramatic increase by

213   ~5.5% from MnCO$_3$-I to -II, in good agreement with Merlini et al. (2015), while the density

214   increased only by ~2% at 35 GPa reported by Boulard et al. (2015). We note that the V/Z at

215   62 GPa measured by Boulard et al. (2015) (corresponding to the red square in Fig. 1) is

216   approximately 2% larger than that from the current EoS of MnCO$_3$-II. Such a large

217   discrepancy may suggest that the unit cell of MnCO$_3$-II in the triclinic system may be

218   overestimated due to the overlap and insufficient diffraction lines in the powder XRD

219   patterns by Boulard et al. (2015).

220

221   **3.2. Vibrational properties of CaCO$_3$ and MnCO$_3$**

222   Four Raman modes were observed in the CaCO$_3$-I phase of CaCO$_3$ and MnCO$_3$, including

223   the translational lattice mode E$_g$ (T), librational lattice mode E$_g$ (L), CO$_3$ in-plane bend mode

224   E$_g$ (v_4), and CO$_3$ symmetric stretch mode A$_{1g}$ (v_1) consistent with previous studies (e.g.,

225   White, 1974; Shi et al., 2012; Farfan et al., 2013). The frequencies of the Raman modes of

226   CaCO$_3$-I at ambient conditions and their pressure dependence (dv/dP) are consistent with

227   literature results (Table 1) (Liu and Mernagh, 1990; Gillet et al., 1993). Calculations show

228   the existence of five Raman peaks with intermediate to strong intensities (Fig. 5 and Table

229   S2). The highest frequency stretching mode E$_g$ (v_3) overlaps with the diamond Raman peak.

230   The frequencies of the Raman modes of MnCO$_3$-I at ambient conditions are consistent with

231   previous work by Shi et al. (2012). The dv/dP of MnCO$_3$-I is comparable to Farfan et al.

232   (2013), although their frequencies are systematically higher by ~10 cm^{-1} possibly caused by

233   the systematic error due to the incorrect setting of the zero position (Table 2).

234

235   The combined XRD and Raman results on CaCO$_3$ and MnCO$_3$ from this study and Merlini et

236   al. (2012b) were used to derive the mode Grüneisen parameters (γ_i). The vibrational

237   frequency (v) as a function of V or P represents the mode Grüneisen parameter for a phonon

238   mode following the relation (Born and Huang, 1954):

239
$$\gamma_i = -\frac{d\ln v}{d\ln V} = \frac{K_T}{v}(\frac{dv}{dP}),$$

240   where K_T is the isothermal bulk modulus. The mode Grüneisen parameters describe the effect

241   that changing the volume of a crystal lattice volume have on its vibrational properties. The γ_i

242   for two external modes (T and L) of MnCO$_3$-I are approximately 2.37 and 1.99, respectively,

243   approximately twice that of CaCO$_3$-I (Tables 1–2). The γ_i for the internal mode v_1 of CaCO$_3$-

244   I is about 0.39, comparable to that for MnCO$_3$-I, FeCO$_3$-I, and MgCO$_3$-I (Liu and Mernagh,

245   1990; Gillet et al., 1993; Lin et al., 2012). The γ_i for the internal mode v_4 of CaCO$_3$-I is

246   approximately 30% less than that of MnCO$_3$-I. The γ_i for v_4 of MnCO$_3$-I of approximately

247   0.33 agrees well with infrared measurements by Boulard et al. (2015), while Santillan and

248   Williams (2004) reported a much smaller γ_i value for the v_4 of MnCO$_3$-I likely due to a large

249   amount of Ca, Fe, and Mg (23 mol% in total) in their rhodochrosite sample. We note that

250   Santillan and Williams (2004) suggested that ion substitution has a negligible effect on IR

251   frequencies (Dubrawski et al., 1989). However, this may be true for the room pressure

252   frequencies and not necessarily true for pressure dependency of IR modes.

253

254   The calculations showed the existence of 75 Raman-active modes in CaCO3-III (Table S3).

255   Most of these modes may overlap in the experimental spectrum. Experimentally we observed

256   19 and 16 Raman bands in $CaCO_3$-III and -VI, respectively. These Raman bands can be

257   assigned to five different Raman modes, including T, L, v_4, v_1, and v_2 (the CO_3 out-of-plane

258   bend). The reduction in frequencies and the modification in the intensity of most of the

259   Raman bands were observed when $CaCO_3$-III transformed into $CaCO_3$-VI at 14-16 GPa,

260   likely a result of the differing orientation of the CO_3^{2-} group in the phases (Fig. 3). $CaCO_3$-III

261   contains non-coplanar CO_3^{2-} groups with a layered structure, while $CaCO_3$-VI is

262   characterized by coplanar CO_3^{2-} groups with a non-layered structure (Merlini et al., 2012b).

263   Williams et al. (1992) may have missed the phase transition from $CaCO_3$-III to -VI due to the

264   large pressure steps for their high-pressure infrared measurements. Fiquet et al. (1994) noted

265   that there were changes in the powder diffraction patterns of $CaCO_3$-III starting near ~8 GPa

266   which might be explained by a new calcite structure, but they could not resolve the new

267   structure and speculated that it could also be related to normal high-pressure features of

268    $CaCO_3$-III. Catalli and Williams (2005) first recognized this phase transition at ~15 GPa and

269   resolved the detailed changes in the carbonate v_4 mode using infrared spectroscopy and finer

270   pressure steps. The lowest-frequency band of $CaCO_3$-III experimentally decreased in

271   frequency with increasing pressure (Fig. 6; Table 1). Raman bands in the same vibrational

272   mode of $CaCO_3$-III seem to have similar values of dv/dP, with <2 for T, approximately 4-6

273   for L, and about 1.3 for v_4. The new band of 866 cm^{-1} at 1.9 GPa was assigned to the v_2 of

274    $CaCO_3$-III, having a negative γ_i and dv/dP of approximately -0.3, which is also observed in

275   calculations (Fig. 6). It is in line with infrared measurements by Williams et al. (1992), which

276   is close to a zero pressure shift of the v_2 of $CaCO_3$-III reported by Catalli and Williams

277   (2005). The negative dv/dP of v_2 could be explained by the increase in the coupling of

278   neighboring CO_3^{2-} groups, while the positive dv/dP of v_4 could be due to an increase in the

279   Mn-O bond strength (Kraft et al., 1991). The dv/dP for the v_1 band decreases approximately

280   by 50% from $CaCO_3$-I to -III.

281

282   Theoretical calculations predict there are 30 active vibrational bands in $CaCO_3$-VI (Fig. 5).

283   14 of them may not be experimentally observed due to their weak intensities at high

284   pressures (see Table S4 for more details). The vibrational modes of high frequencies at 1400-

285   1650 cm^{-1} were not experimentally observed in this study because of their superposition with

286   the diamond Raman peak. The v_1 of $CaCO_3$-VI from theoretical calculations agree perfectly

287   with experiment observations (Fig. 6). Both suggested that the dv/dP for the v_1 band

288   decreases approximately by 30% from $CaCO_3$-III to -VI. Furthermore, one v_2 band of

289     $CaCO_3$-III diverged into two v_2 bands of $CaCO_3$-VI, while theoretical calculations only

290   predict one v_2 band with a small positive dv/dP value close to zero. For $CaCO_3$-VI, the lower-

291   frequency v_2 band of 860 cm^{-1} experimentally had a negative dv/dP of approximately -0.5,

292   but the higher-frequency v_2 band of 867 cm^{-1} had a positive dv/dP of approximately +0.3. We

293   note that Catalli and Williams (2005) observed one v_2 peak of $CaCO_3$-VI having an

294   unchanged position of near 870 cm^{-1} throughout infrared measurements up to 52 GPa. The

295   dv/dP values of $CaCO_3$-VI for the T bands from experimental measurements are around 2,

296   for the L bands at 2-3.5, and for the v_4 bands approximately at 1.2, which are comparable to

297   those from theoretical calculations.

298

299   Although they are isostructural, the number and relative intensity of the Raman bands

300   observed in $MnCO_3$-II are not the same as $CaCO_3$-VI (Figs. 3–4). The difference in the

301   Raman spectra of the $CaCO_3$-VI-structured $CaCO_3$ and $MnCO_3$ suggests that cations (e.g.,

302   Mn^{2+} and Ca^{2+}) can have more dramatic effects on the vibrational modes in the high-pressure

303    $CaCO_3$-VI phase than the rhombohedral $CaCO_3$-I phase. All 13 Raman bands of $MnCO_3$-II

304   monotonically increased in frequency with increasing pressure (Fig. 7; Table 2). The dv/dP

305   of $MnCO_3$-II for the T bands are at 1-2 and for the L bands at 2-2.5. All the T and L Raman

306   bands have the value of γ_i at ~2. Three Raman bands for $MnCO_3$-II in 700–850 cm^{-1} display a

307   comparable dv/dP of ~0.55 and γ_i of ~0.28, and were thus assigned to v_4. The v_2 band at 873

308   cm^{-1} only appears between 44 and 47 GPa, and likely becomes too weak after the completion

309   of the phase transformation to $MnCO_3$-II to be observed. The Raman spectra collected at 44–

310   47 GPa exhibit the peak splitting of Raman bands within the pressure range where we

311   observed coexistence of $MnCO_3$-I and -II according to X-ray diffraction patterns (Figs. 1

312   insert and 4). Two v_1 Raman bands were observed at 46 GPa, likely with one coming from

313    $MnCO_3$-I and the other from $MnCO_3$-II. Farfan et al. (2013) observed such splitting of v_1

314   from 48.2 to 55.2 GPa, indicating that $MnCO_3$-I and -II coexisted at a larger pressure range

315   due to the use of silicon oil as the pressure-transmitting medium. The dv/dP of v_1 for

316    $MnCO_3$-II is about 1.72, in good agreement with the infrared measurements by Boulard et al.

317   (2015). We note that Raman peak splitting in $MnCO_3$-I at 44-47 GPa might suggest a subtle

318   distortion of the $CaCO_3$-I structure between $MnCO_3$-I and -II, which may be similar to the

319   change from the $CaCO_3$-III and $CaCO_3$-IIIb structures (Merlini et al., 2012b), although this

320   potential transition cannot be resolved from the present diffraction patterns in this study.

321

4. Implications

The phase stability of divalent metal carbonates (MCO_3) is significantly affected by compositional variation in the metal cations (M^{2+}). Previous studies suggested the $CaCO_3$-I phase stability of the $(Mn,Ca)CO_3$ solid solution was greatly enhanced by adding Mn^{2+} (Shi et al., 2012). For the Mn-rich $(Mn,Ca)CO_3$ compositions, the solid solution may directly transform into the $CaCO_3$-VI structure without going through $CaCO_3$-II and -III at high pressures (Fig. 8) (Boulard et al., 2015; Merlini et al., 2015). The phase transition pressure for $MnCO_3$ increased by approximately 2-3 GPa with an additional 2 mol% Mn^{2+} and 1 mol% Fe^{2+} replacing Ca^{2+} in $(Mn_{0.96}Ca_{0.04})CO_3$ (Merlini et al., 2015). The presence of 7 mol% Mg^{2+} and 9 mol% Fe^{2+} in $(Mn,Ca)CO_3$ could stabilize the $CaCO_3$-I phase at ~50 GPa and 2000 K (Santillan and Williams, 2004). Furthermore, $MgCO_3$ can stabilize the $CaCO_3$-I structure up to at least 110 GPa at 2000 K (Isshiki et al., 2004), while $FeCO_3$ undergoes an isostructural spin transition around 45 GPa and remains in the $CaCO_3$-I structure to above 100 GPa at ambient temperature (e.g., Lavina et al., 2010; Farfan et al., 2012; Liu et al., 2014; Liu et al., 2015). In $(Mn,Ca)CO_3$, the radii of Ca^{2+} (100 pm) and Mn^{2+} (83 pm) are greater than that of Mg^{2+} (72pm) and Fe^{2+} (78 and 61 pm for the high-spin and low-spin states, respectively) (Shannon, 1976). The incorporation of a smaller cation into $CaCO_3$ increases the stability field of $CaCO_3$-I (Fig. 9).

The phase stability and high-pressure polymorph(s) of divalent metal carbonates (MCO_3) under Earth's mantle conditions have been an area of active debate. The lower-mantle oxygen fugacity may be at the Ni/NiO or Fe/FeO buffers making carbonates unstable in the deep mantle (see review by Frost and McCammon (2008)). However, considering the

345   uncertainty in our knowledge of lower-mantle oxygen fugacity, carbonates may be

346   transported into the lower mantle by subducting slabs if the local oxygen fugacity is

347   favorable for their survival. One piece of evidence is the observation of carbonate-bearing

348   inclusions in diamonds which were potentially brought up to the Earth's surface from the

349   deep mantle (Berg, 1986; Wang et al., 1996; Walter et al., 2011). The high-pressure

350   polymorph $CaCO_3$-VI has a smaller V/Z than aragonite up to at least 40 GPa and may replace

351   aragonite in the Earth's mantle (Merlini et al., 2012b). The $CaCO_3$-VI-structured

352    $(Ca,Mn)CO_3$ is stable up to at least 75 GPa at room temperature according to Raman spectra

353   in this study. The incorporation of smaller cations (e.g., Mg^{2+}, Fe^{2+}, and Mn^{2+}) can

354   significantly reduce the V/Z of $CaCO_3$-I and -VI, and thus may enhance the stability field of

355    $CaCO_3$-rich carbonate in the $CaCO_3$-I and -VI structures inside cold, subducting slabs in the

356   deep mantle that carried various limestone and carbonaceous sediments.

357

References

Baroni, S., de Gironcoli, S., Dal Corso, A., and Giannozzi, P. (2001) Phonons and related crystal properties from density-functional perturbation theory. Review of Modern Physics, 73, 515-562.

Baroni, S., and Resta, R. (1986) Ab initio calculation of the low-frequency Raman cross section in silicon. Physical Review B, 33, 5969-5971.

Berg, G.W. (1986) Evidence for carbonate in the mantle. Nature, 324(6092), 50-51.

Biellmann, C., Gillet, P., Guyot, F.o., Peyronneau, J., and Reynard, B. (1993) Experimental evidence for carbonate stability in the Earth's lower mantle. Earth and Planetary Science Letters, 118(1–4), 31-41.

Born, M., and Huang, K. (1954) Dynamical theory of crystal lattices. Oxford University Press, U.K.

Boulard, E., Goncharov, A.F., Blanchard, M., and L. Mao, W. (2015) Pressure-induced phase transition in $MnCO_3$ and its implications on the deep carbon cycle. Journal of Geophysical Research: Solid Earth, 120(6), 4069-4079.

Caracas, R., and Bobocioiu, E. (2011) The WURM project - a freely available web-based repository of computed physical data for minerals. American Mineralogist, 96, 437-444.

Catalli, K., and Williams, Q. (2005) A high-pressure phase transition of calcite-III. American Mineralogist, 90(10), 1679-1682.

Dasgupta, R., and Hirschmann, M.M. (2010) The deep carbon cycle and melting in Earth's interior. Earth and Planetary Science Letters, 298(1–2), 1-13.

Dera, P., Zhuravlev, K., Prakapenka, V., Rivers, M.L., Finkelstein, G.J., Grubor-Urosevic, O., Tschauner, O., Clark, S.M., and Downs, R.T. (2013) High pressure single-crystal micro X-ray diffraction analysis with GSE_ADA/RSV software. High Pressure Research, 33(3), 466-484.

Dubrawski, J.V., Channon, A.-L., and Warne, S.S. (1989) Examination of the siderite-magnesite mineral series by Fourier transform infrared spectroscopy. American Mineralogist, 74, 187-190.

Farfan, G., Wang, S., Ma, H., Caracas, R., and Mao, W.L. (2012) Bonding and structural changes in siderite at high pressure. American Mineralogist, 97(8-9), 1421-1426.

Farfan, G.A., Boulard, E., Wang, S., and Mao, W.L. (2013) Bonding and electronic changes in rhodochrosite at high pressure. American Mineralogist, 98(10), 1817-1823.

Fei, Y., Ricolleau, A., Frank, M., Mibe, K., Shen, G., and Prakapenka, V. (2007) Toward an internally consistent pressure scale. Proceedings of the National Academy of Sciences, 104(22), 9182-9186.

Fiquet, G., Guyot, F., and Itie, L.P. (1994) High-pressure X-ray diffraction study of carbonates: $MgCO_3$, $CaMg(CO_3)_2$, and $CaCO_3$. American Mineralogist, 79, 15-23.

Fiquet, G., Guyot, F., Kunz, M., Matas, J., Andrault, D., and Hanfland, M. (2002) Structural refinements of magnesite at very high pressure. American Mineralogist, 87(8-9), 1261-1265.

Frost, D.J., and McCammon, C.A. (2008) The redox state of Earth's mantle. Annual Review of Earth and Planetary Sciences, 36(1), 389-420.

Fuchs, M., and Scheffler, M. (1999) Ab initio pseudopotentials for electronic structure calculations of poly-atomic systems using density-functional theory. Computer Physics Communications, 119, 67-98.

424

425

426   Gillet, P., Biellmann, C., Reynard, B., and McMillan, P. (1993) Raman spectroscopic studies
427   of carbonates part I: High-pressure and high-temperature behaviour of calcite, magnesite,
428   dolomite and aragonite. Physics and Chemistry of Minerals, 20(1), 1-18.
429   Gonze, X., Amadon, B., Anglade, P.M., Beuken, J.M., Bottin, F., Boulanger, P., Bruneval, F.,
430   Caliste, D., Caracas, R., Côté, M., Deutsch, T., Genovese, L., Ghosez, P., Giantomassi,
431   M., Goedecker, S., Hamann, D.R., Hermet, P., Jollet, F., Jomard, G., Leroux, S., Mancini,
432   M., Mazevet, S., Oliveira, M.J.T., Onida, G., Pouillon, Y., Rangel, T., Rignanese, G.M.,
433   Sangalli, D., Shaltaf, R., Torrent, M., Verstraete, M.J., Zerah, G., and Zwanziger, J.W.
434   (2009) ABINIT: First-principles approach to material and nanosystem properties.
435   Computer Physics Communications, 180(12), 2582-2615.
436   Gonze, X., Rignanese, G.-M., and Caracas, R. (2005) First-principles studies of the lattice
437   dynamics of crystals, and related properties. Zeitschrift fu r Kristallographie, 220, 458-
438   472.
439   Graf, D. L. (1961) Crystallographic tables for the rhombohedral carbonates. American
440   Mineralogist, 46, 1283-1316.
441   Hazen, R.M., and Schiffries, C.M. (2013) Why deep carbon? Reviews in Mineralogy and
442   Geochemistry, 75(1), 1-6.
443   Ishizawa, N., Setoguchi, H., and Yanagisawa, K. (2013) Structural evolution of calcite at
444   high temperatures: Phase V unveiled. Scientific Reports, 3, 2832.
445   Isshiki, M., Irifune, T., Hirose, K., Ono, S., Ohishi, Y., Watanuki, T., Nishibori, E., Takata,
446   M., and Sakata, M. (2004) Stability of magnesite and its high-pressure form in the
447   lowermost mantle. Nature, 427(6969), 60-63.
448   Kraft, S., Knittle, E., and Williams, Q. (1991) Carbonate stability in the Earth's mantle: A
449   vibrational spectroscopic study of aragonite and dolomite at high pressures and
450   temperatures. Journal of Geophysical Research, 96(B11), 17997-18009.
451   Lavina, B., Dera, P., Downs, R.T., Yang, W., Sinogeikin, S., Meng, Y., Shen, G., and
452   Schiferl, D. (2010) Structure of siderite $FeCO_3$ to 56 GPa and hysteresis of its spin-
453   pairing transition. Physical Review B, 82(6), 064110.
454   Lin, J.-F., Liu, J., Jacobs, C., and Prakapenka, V.B. (2012) Vibrational and elastic properties
455   of ferromagnesite across the electronic spin-pairing transition of iron. American
456   Mineralogist, 97(4), 583-591.
457   Litasov, K.D., Fei, Y., Ohtani, E., Kuribayashi, T., and Funakoshi, K. (2008) Thermal
458   equation of state of magnesite to 32 GPa and 2073 K. Physics of the Earth and Planetary
459   Interiors, 168(3–4), 191-203.
460   Liu, J., Lin, J.-F., Mao, Z., and Prakapenka, V.B. (2014) Thermal equation of state and spin
461   transition of magnesiosiderite at high pressure and temperature. American Mineralogist,
462   99(1), 84-93.
463   Liu, J., Lin, J.-F., and Prakapenka, V.B. (2015) High-pressure orthorhombic ferromagnesite
464   as a potential deep-mantle carbon carrier. Scientific Reports, 5, 7640.
465   Liu, L.-g., Lin, C.-C., and Yang, Y.-J. (2001) Formation of diamond by decarbonation of
466   MnCO3. Solid State Communications, 118(4), 195-198.
467   Liu, L.-G., and Mernagh, T.P. (1990) Phase transitions and Raman spectra of calcite at high
468   pressures and room temperature. American Mineralogist, 75(7-8), 801-806.

469   Mao, H.-K., Xu, J., and Bell, P.M. (1986) Calibration of the ruby pressure gauge to 800 kbar
470   under quasi-hydrostatic conditions. Journal of Geophysical Research, 91(B5), 4673-4676.
471   Merlini, M., Crichton, W.A., Hanfland, M., Gemmi, M., Müller, H., Kupenko, I., and
472   Dubrovinsky, L. (2012a) Structures of dolomite at ultrahigh pressure and their influence
473   on the deep carbon cycle. Proceedings of the National Academy of Sciences, 109(34),
474   13509-13514.
475   Merlini, M., Hanfland, M., and Crichton, W.A. (2012b) $CaCO_3$-III and $CaCO_3$-VI, high-
476   pressure polymorphs of calcite: Possible host structures for carbon in the Earth's mantle.
477   Earth and Planetary Science Letters, 333–334, 265-271.
478   Merlini, M., Hanfland, M., and Gemmi, M. (2015) The $MnCO_3$-II high-pressure polymorph
479   of rhodocrosite. American Mineralogist, 100(11-12), 2625-2629.
480   Monkhorst, H.J., and Pack, J.D. (1976) Special points for Brillouin-zone integrations.
481   Physical Review B, 13(12), 5188-5192.
482   Oganov, A.R., Glass, C.W., and Ono, S. (2006) High-pressure phases of $CaCO_3$: Crystal
483   structure prediction and experiment. Earth and Planetary Science Letters, 241(1–2), 95-
484   103.
485   Ono, S. (2007) High-pressure phase transformation in $MnCO_3$: a synchrotron XRD study.
486   Mineralogical Magazine, 71(1), 105-111.
487   Ono, S., Kikegawa, T., and Ohishi, Y. (2007) High-pressure transition of $CaCO_3$. American
488   Mineralogist, 92(7), 1246-1249.
489   Ono, S., Kikegawa, T., Ohishi, Y., and Tsuchiya, J. (2005) Post-aragonite phase
490   transformation in $CaCO_3$ at 40 GPa. American Mineralogist, 90(4), 667-671.
491   Pippinger T., Miletich R., Merlini M., Lotti P., Schouwink P., Yagi T., Crichton W.A.,
492   Hanfland M. (2015) Puzzling calcite-III dimorphism: Crystallography, high-pressure
493   behavior, and pathway of single-crystal transitions. Physics and Chemistry of Minerals
494   42, 29-43.
495   Prescher, C., and Prakapenka, V.B. (2015) DIOPTAS: a program for reduction of two-
496   dimensional X-ray diffraction data and data exploration. High Pressure Research, 35(3),
497   223-230.
498   Santillan, J., and Williams, Q. (2004) A high-pressure infrared and X-ray study of $FeCO_3$ and
499         $MnCO_3$: comparison with $CaMg(CO_3)_2$-dolomite. Physics of the Earth and Planetary
500   Interiors, 143–144, 291-304.
501   Shannon, R.D. (1976) Revised effective ionic radii and systematic studies of interatomic
502   distances in halides and chalcogenides. Acta Crystallographica Section A, 32(5), 751-767.
503   Shi, W., Fleet, M.E., and Shieh, S.R. (2012) High-pressure phase transitions in Ca-Mn
504   carbonates (Ca,Mn)CO3 studied by Raman spectroscopy. American Mineralogist, 97(5-
505   6), 999-1001.
506   Suito, K., Namba, J., Horikawa, T., Taniguchi, Y., Sakurai, N., Kobayashi, M., Onodera, A.,
507   Shimomura, O., and Kikegawa, T. (2001) Phase relations of $CaCO_3$ at high pressure and
508   high temperature. American Mineralogist, 86(9), 997-1002.
509   Veithen, M., Gonze, X., and Ghosez, P. (2005) Nonlinear optical susceptibilities, Raman
510   efficiencies, and electro-optic tensors from first-principles density functional perturbation
511   theory. Physical Review B, 71(12), 125107.
512   Walter, M.J., Kohn, S.C., Araujo, D., Bulanova, G.P., Smith, C.B., Gaillou, E., Wang, J.,
513   Steele, A., and Shirey, S.B. (2011) Deep mantle cycling of oceanic crust: evidence from
514   diamonds and their mineral inclusions. Science, 334(6052), 54-57.

515   Wang, A., Pasteris, J.D., Meyer, H.O.A., and Dele-Duboi, M.L. (1996) Magnesite-bearing
516   inclusion assemblage in natural diamond. Earth and Planetary Science Letters, 141(1–4),
517   293-306.
518   White, W.B. (1974) The carbonate minerals. In V.C. Farmer, Ed. Infrared spectra of minerals,
519   p. 227-284. Mineralogical Society of Great Britain & Ireland, London.
520   Williams, Q., Collerson, B., and Knittle, E. (1992) Vibrational spectra of magnesite ($MgCO_3$)
521   and calcite-III at high pressures. American Mineralogist, 77(11-12), 1158-1165.
522   Zhang, J., Martinez, I., Guyot, F., and Reeder, R.J. (1998) Effects of Mg-Fe^{2+} substitution in
523   calcite-structure carbonates: thermoelastic properties. American Mineralogist, 83(3-4),
524   280-287.
525   Zhang, J., and Reeder, R.J. (1999) Comparative compressibilities of calcite-structure
526   carbonates: Deviations from empirical relations. American Mineralogist, 84(5-6), 861-
527   870.
528

Figure Captions

FIGURE 1. The pressure-volume relations of $MnCO_3$-I and -II. Insert: X-ray diffraction images collected during a rotation of 30° at 32, 47, and 67 GPa, respectively, showing the sharp diffraction peaks of $MnCO_3$ at high pressures. The diffraction rings in the XRD patterns were from the pressure medium Ne while the $MnCO_3$ single crystal remained across the phase transition. The diffraction images were illustrated by the DIOPTAS program (Prescher and Prakapenka, 2015). Circles and diamonds: the unit cell volume per formula (V/Z) for $MnCO_3$-I and -II from this study; square and triangles: V/Z of $MnCO_3$-II by Boulard et al. (2015) and Merlini et al. (2015), respectively; lines: BM EoS fits to the data. Error bars smaller than symbols are not shown for clarity. See Table S1 in Supplementary Materials for more details.

FIGURE 2. The relative axial compressibilities of the rhombohedral phase of $MnCO_3$-I as a function of pressure. Circles, squares, diamonds, and triangles: c/a, a/a_0, c/c_0, and V/V_0, respectively. Error bars smaller than symbols are not shown for clarity.

FIGURE 3. Representative Raman spectra of $CaCO_3$ at high pressures and 300 K. The metastable $CaCO_3$-II phase was not observed likely due to the small pressure range over which this phase is stable and the relatively large pressure steps. Raman modes of $CaCO_3$-I are labeled according to White (1974). T: translational lattice mode; L: librational lattice mode; v_4: CO_3 in-plane bend; v_2: CO_3 out-of-plane bend; v_1: CO_3 symmetric stretch.

551 **FIGURE 4.** Representative Raman spectra of $MnCO_3$ at high pressures. $MnCO_3$ transformed

552 from the low-pressure phase ($MnCO_3$-I) to the high-pressure phase ($MnCO_3$-II) at 44-47 GPa.

553 Raman modes of $MnCO_3$-I are labeled accordingly as T, L, v_4, and v_1. The splitting of Raman

554 bands of $MnCO_3$ at 46 GPa corresponds to the coexisting phases of I and II revealed by XRD

555 measurements at 47 GPa (Fig. 1 insert) with the v_2 peak possibly at ~875 cm^{-1}.

556

557 **FIGURE 5.** Vibrational modes of $CaCO_3$-I and VI as a function of frequency at high

558 pressures by theoretical calculations. The intensity was normalized using the intensity of v_1

559 as the reference. The blues diamonds indicate that the calculated intensity of modes are

560 extremely weak (see Tables S2 and S4 in Supplementary Materials for more details).

561

562 **FIGURE 6.** Raman shifts of $CaCO_3$ at high pressures. Black, blue, and red symbols:

563 experimental observations of $CaCO_3$-I, -III, and -VI, respectively; olive diamonds, triangles,

564 and squares: theoretical calculations of $CaCO_3$-I, -III, and -VI, respectively (this study). The

565 calculated modes with the extremely weak intensities (blue diamonds in Fig. 5) are not

566 shown for clarity. The calculated 75 Raman peaks of $CaCO_3$-III were selectively plotted for

567 comparison. Two vertical dotted lines approximately display the phase transition pressures.

568 The solid lines represent the linear fits to the calculations. Error bars are typically smaller

569 than symbols. See Tables S2-S5 in Supplementary Materials for more details.

570

571 **FIGURE 7.** Raman shifts of $MnCO_3$ at high pressures. Solid, half-filled, and open symbols:

572 $MnCO_3$-I, the coexisting phases of I and II, and $MnCO_3$-II, respectively; blue shaded area:

573 the coexisting phases of I and II; solid lines: linear fits to experimental data. Error bars are

574   typically smaller than symbols and are not shown for clarity. See Table S6 in Supplementary

575   Materials for more details.

576
577   **FIGURE 8.** Schematic phase relations of the $(Mn,Ca)CO_3$ solid-solution series at 300 K.

578   Dashed lines represent the tentative phase boundaries. Solid triangles: this study; diamonds:

579   Merlini et al. (2012, 2015); squares and circles: Shi et al. (2012).

580

581   **FIGURE 9.** Schematic phase relations of the $(Ca,Mn,Fe,Mg)CO_3$ solid-solution system

582   under high pressures at 300 K. The effective ionic radii of Ca^{2+}, Mn^{2+}, Fe^{2+}, and Mg^{2+} at

583   ambient conditions are illustrated accordingly from Shannon (1976). *hs*: the high-spin state

584   of Fe^{2+}; *ls*: the low-spin state of Fe^{2+}.

585   **Table 1.** Experimental vibrational parameters of $CaCO_3$ at high pressures

$CaCO_3$	Raman mode	Initial frequency* (cm^{-1})	$d\nu/dP$ (cm^{-1}/GPa)	Mode Grüneisen parameter (γ_i)
I	T	156	2.52(8)	1.14(4)
I	L	282	5.19(17)	1.33(6)
I	ν_4	713	2.35(7)	0.23(1)
I	ν_1	1086	5.96(15)	0.39(2)
III	T	131	-0.35(6)	-0.34(7)
III	T	140	1.98(10)	1.66(9)
III	T	161	0.76(11)	0.56(9)
III	T	168	0.36(6)	0.25(5)
III	T	202	0.56(4)	0.35(4)
III	T	206	0.89(13)	0.52(9)
III	T	219	1.91(21)	1.04(13)
III	L	242	3.78(18)	1.78(11)
III	L	256	4.41(29)	1.90(15)
III	L	266	4.32(17)	1.82(9)
III	L	275	6.31(26)	2.46(12)
III	L	296	5.76(25)	2.17(11)
III	L	312	6.25(33)	2.21(17)
III	L	330	6.28(32)	2.08(15)
III	ν_4	689	1.35(8)	0.23(2)
III	ν_4	731	1.31(17)	0.22(3)
III	ν_4	739	1.33(17)	0.22(3)
III	ν_2	866	-0.29(3)	-0.04(1)
III	ν_1	1102	2.78(14)	0.31(3)
VI	T	150	0.01(1)	0.01(1)
VI	T	172	1.37(22)	1.56(30)
VI	T	180	2.87(45)	3.03(57)
VI	T	195	2.17(49)	2.22(55)
VI	T	245	2.06(21)	1.81(20)
VI	L	284	2.04(26)	1.54(21)
VI	L	329	2.21(57)	1.48(46)
VI	L	343	1.98(62)	1.29(45)
VI	L	356	3.08(33)	1.83(24)
VI	L	382	2.82(29)	1.62(20)
VI	L	391	3.45(21)	1.87(15)
VI	ν_4	732	1.19(9)	0.39(5)
VI	ν_4	746	1.19(9)	0.39(5)
VI	ν_2	860	-0.48(7)	-0.14(3)
VI	ν_2	867	0.33(7)	0.09(2)
VI	ν_1	1134	2.04(12)	0.44(3)

586   *Initial frequencies of Raman modes for CaCO3-I, -III, and -VI are at 0, 1.9, and 16 GPa,
587   respectively.
588

589 **Table 2.** Experimental vibrational parameters of $MnCO_3$ at high pressures

$MnCO_3$	Raman mode	Initial frequency* (cm^{-1})	$d\nu/dP$ (cm^{-1}/GPa)	Mode Grüneisen parameter (γ_i)
I	T	184	2.91(5)	2.37(7)
I	L	290	3.68(9)	1.99(8)
I	ν_4	719	1.28(6)	0.33(3)
I	ν_1	1086	2.17(7)	0.38(3)
II	T	165	0.89(6)	1.93(17)
II	T	203	1.09(8)	1.91(19)
II	T	220	1.33(10)	2.15(18)
II	T	244	1.01(8)	1.50(14)
II	T	324	1.83(5)	2.02(8)
II	L	391	2.05(11)	1.87(11)
II	L	442	2.12(21)	1.72(19)
II	L	481	2.70(16)	2.01(19)
II	L	503	2.48(19)	1.78(22)
II	ν_4	735	0.51(4)	0.26(4)
II	ν_4	782	0.58(10)	0.28(6)
II	ν_4	826	0.63(8)	0.29(5)
II	ν_1	1202	1.72(8)	0.54(9)

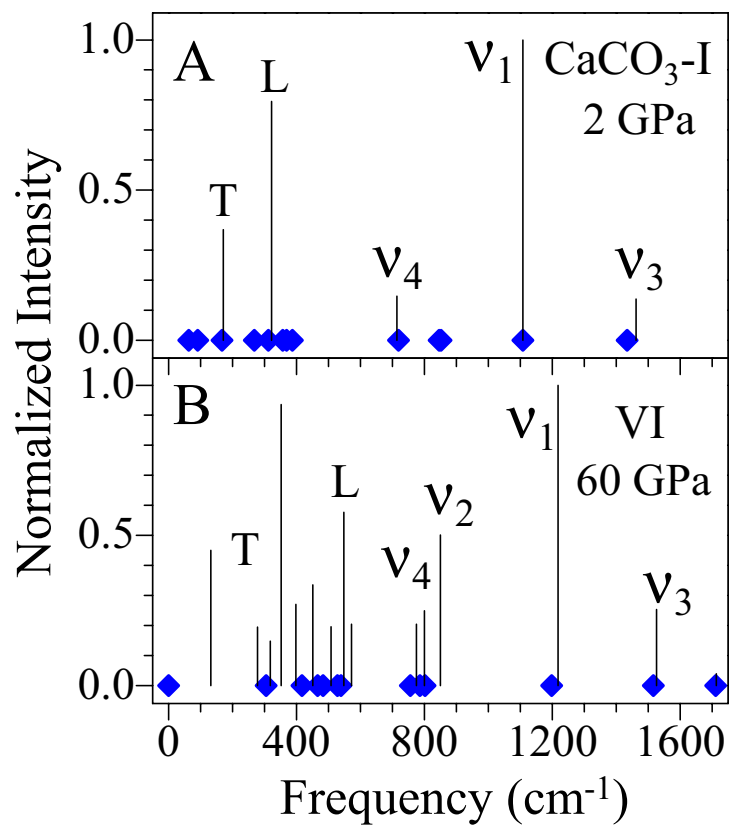590 *Initial frequencies of Raman modes for MnCO3-I and -II are at 0 and 48 GPa, respectively.
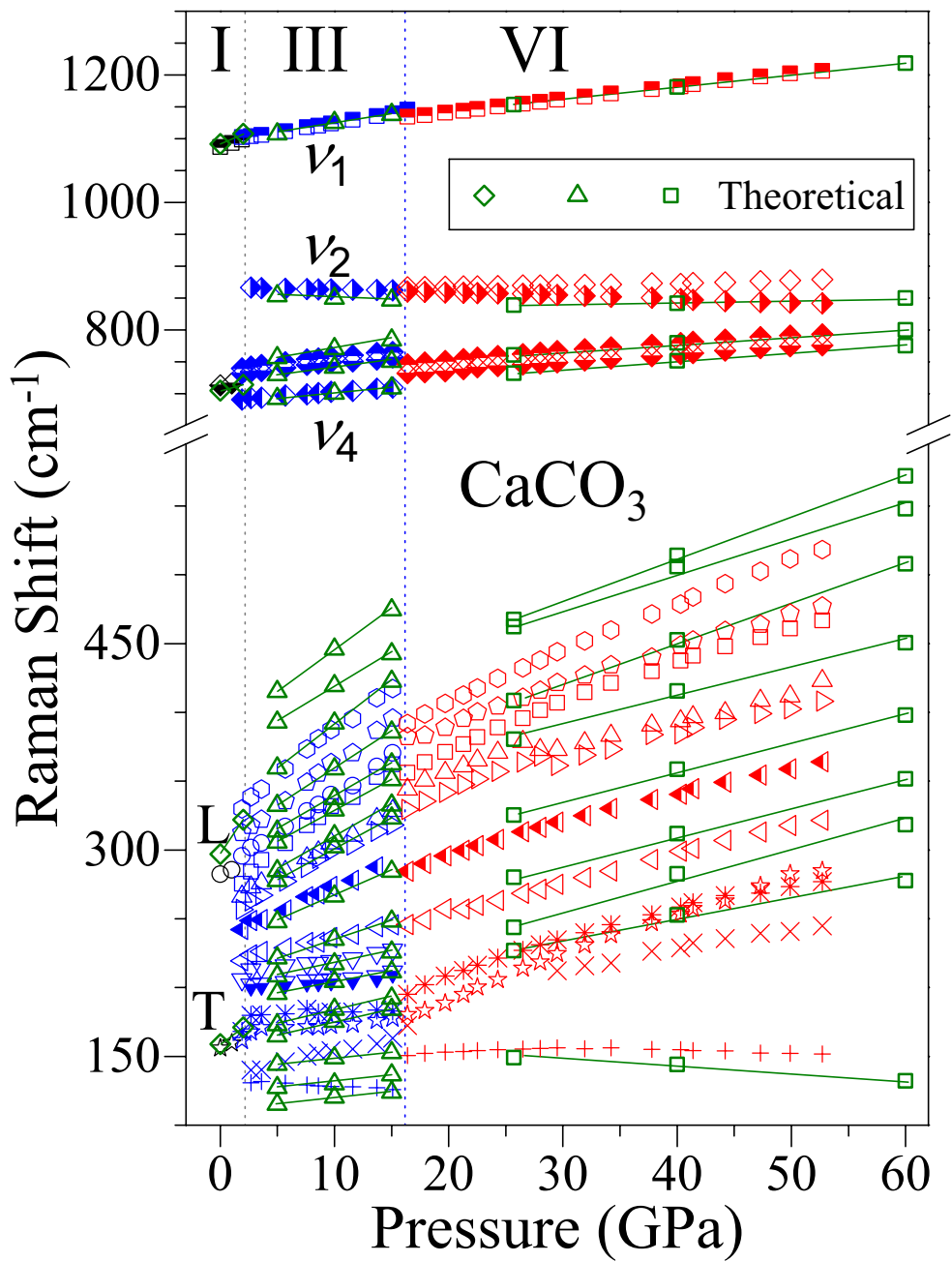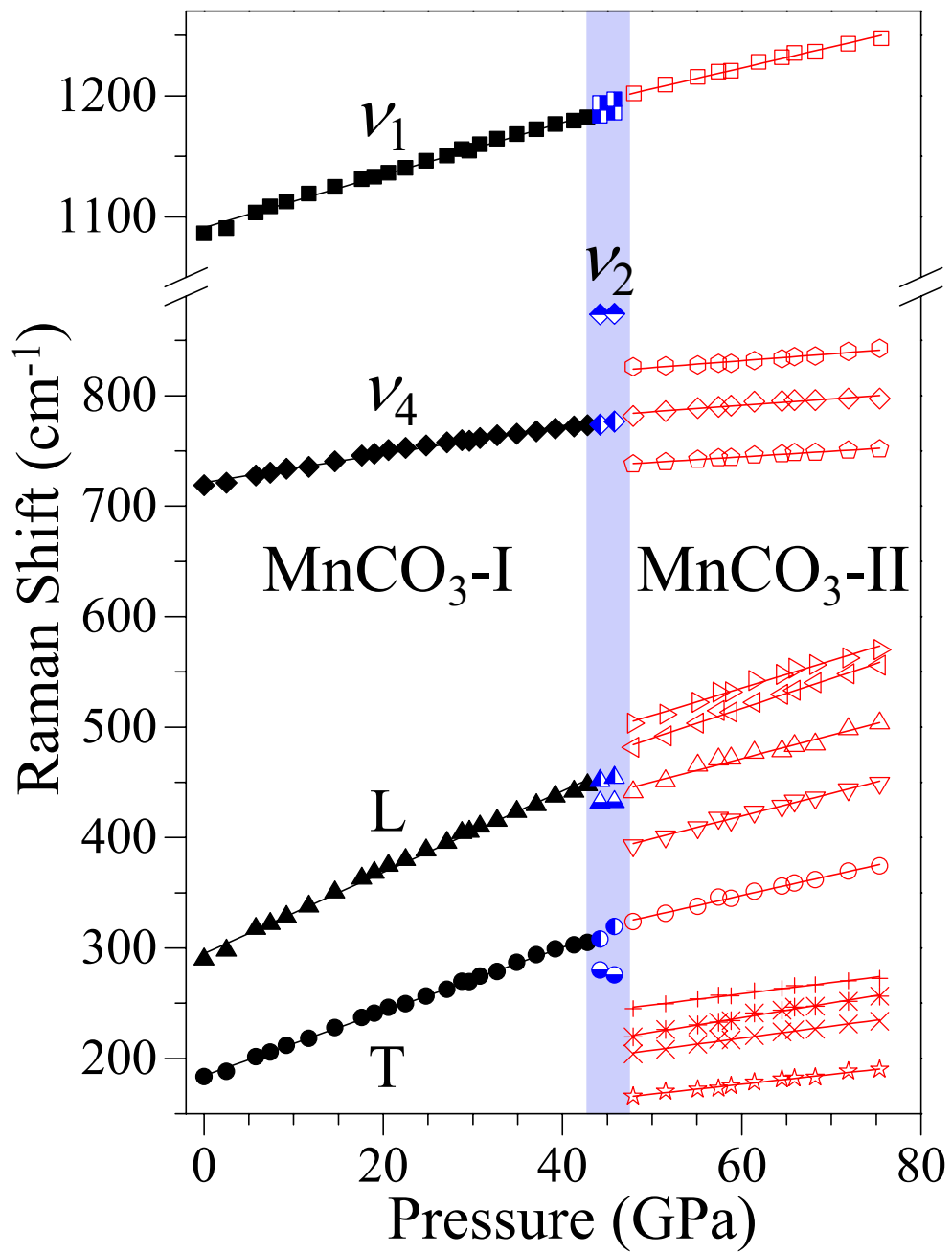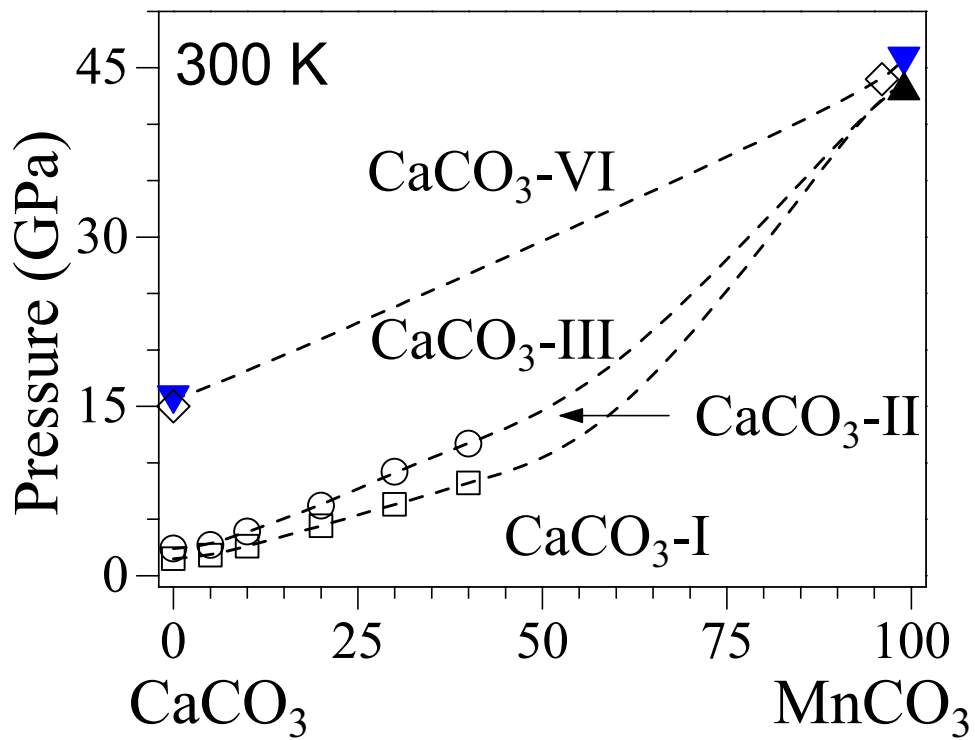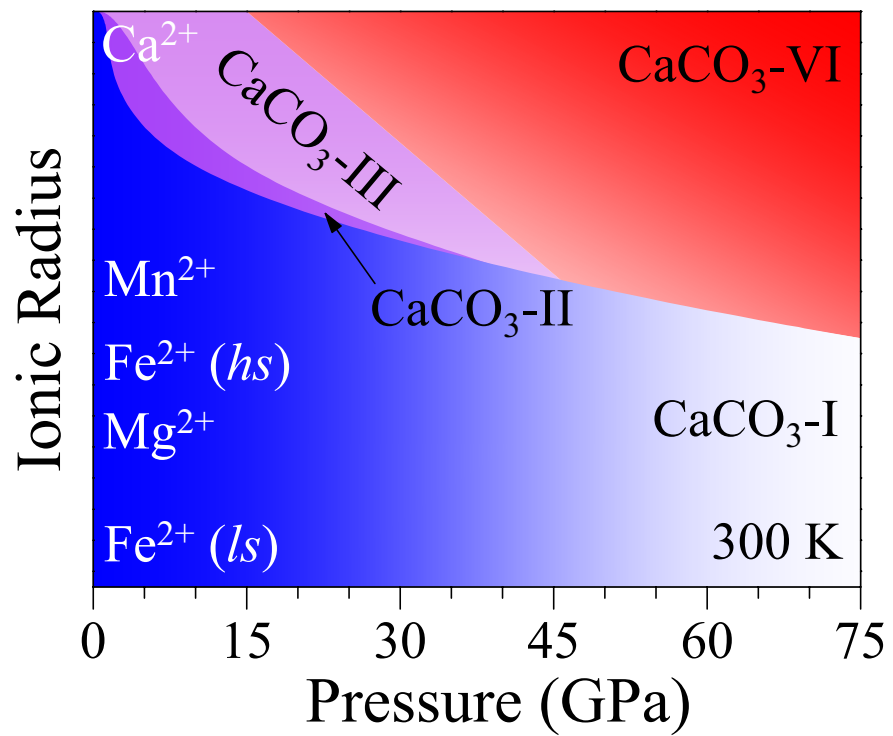591
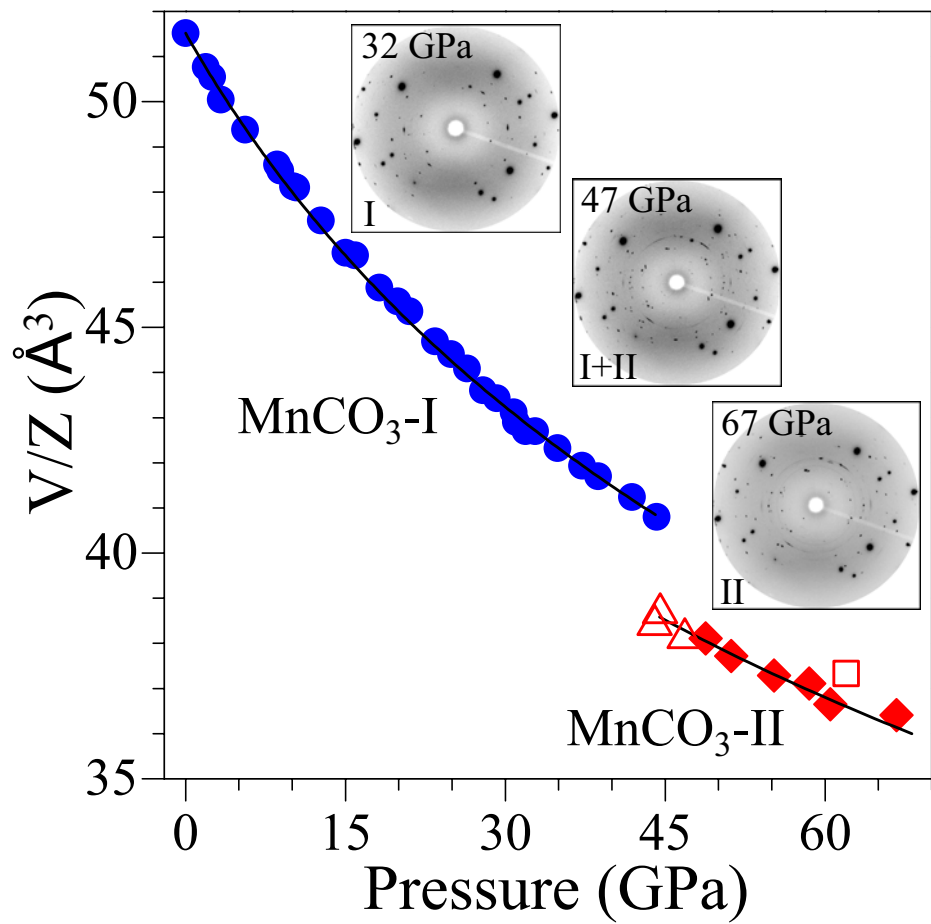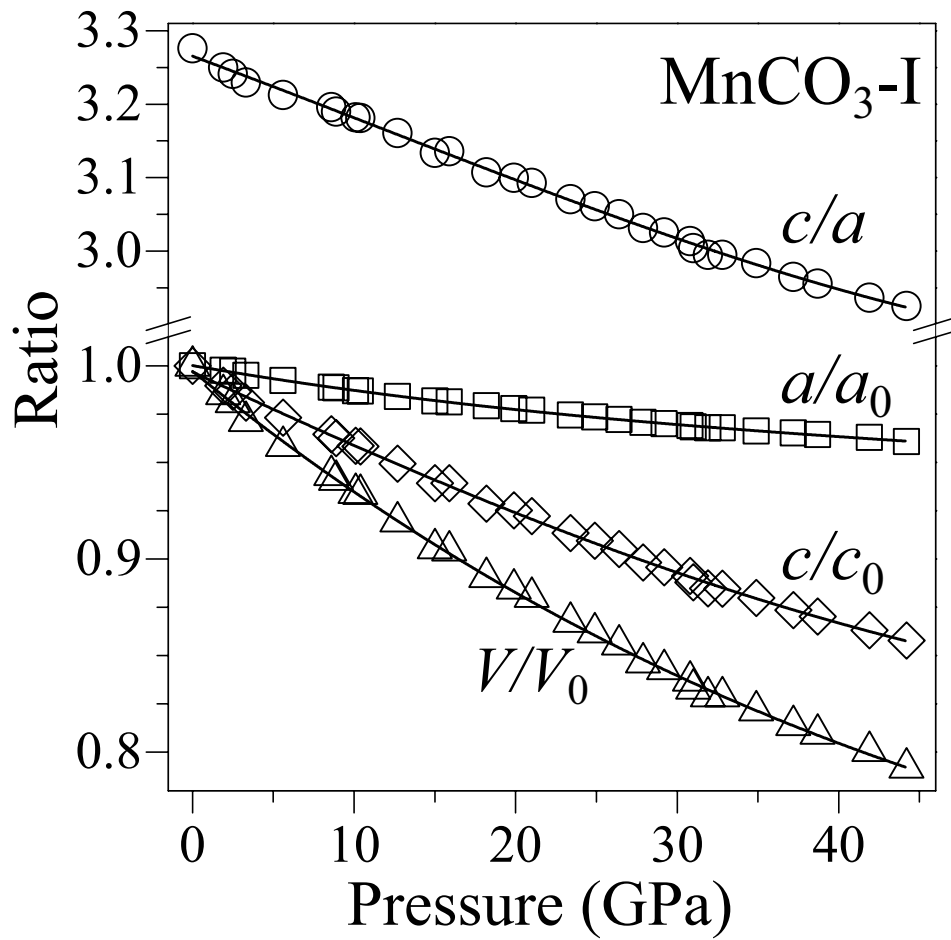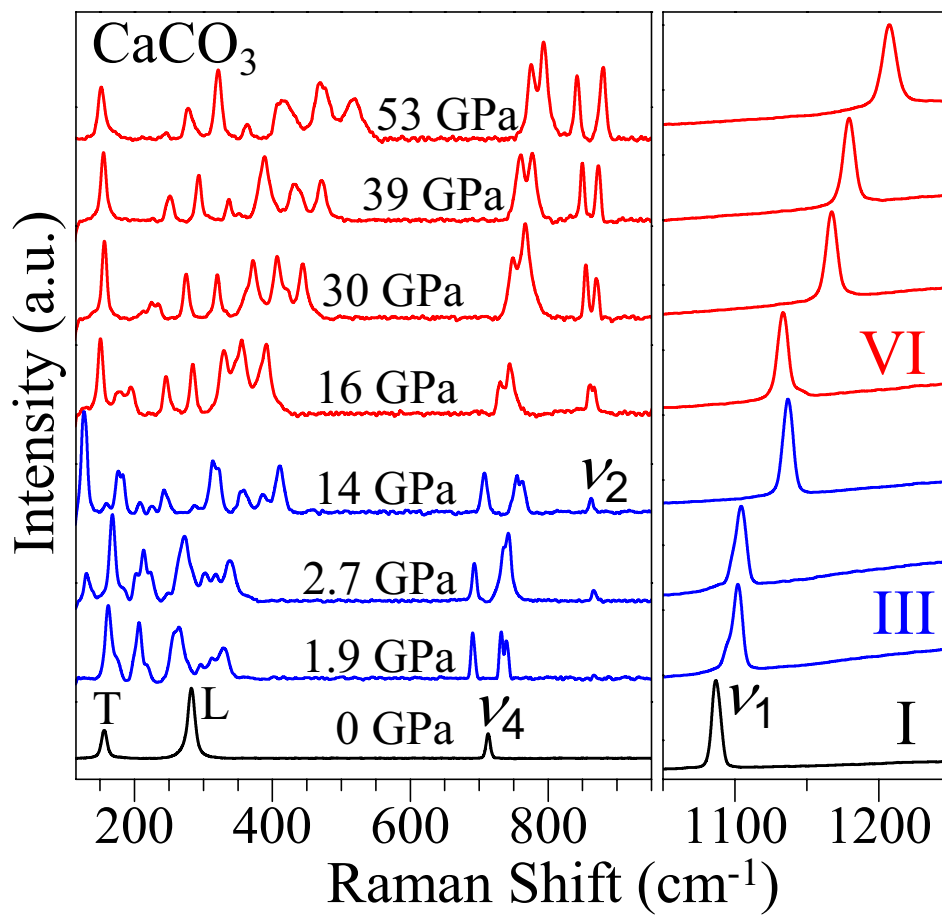
Figure 1

Figure 2

Figure 3
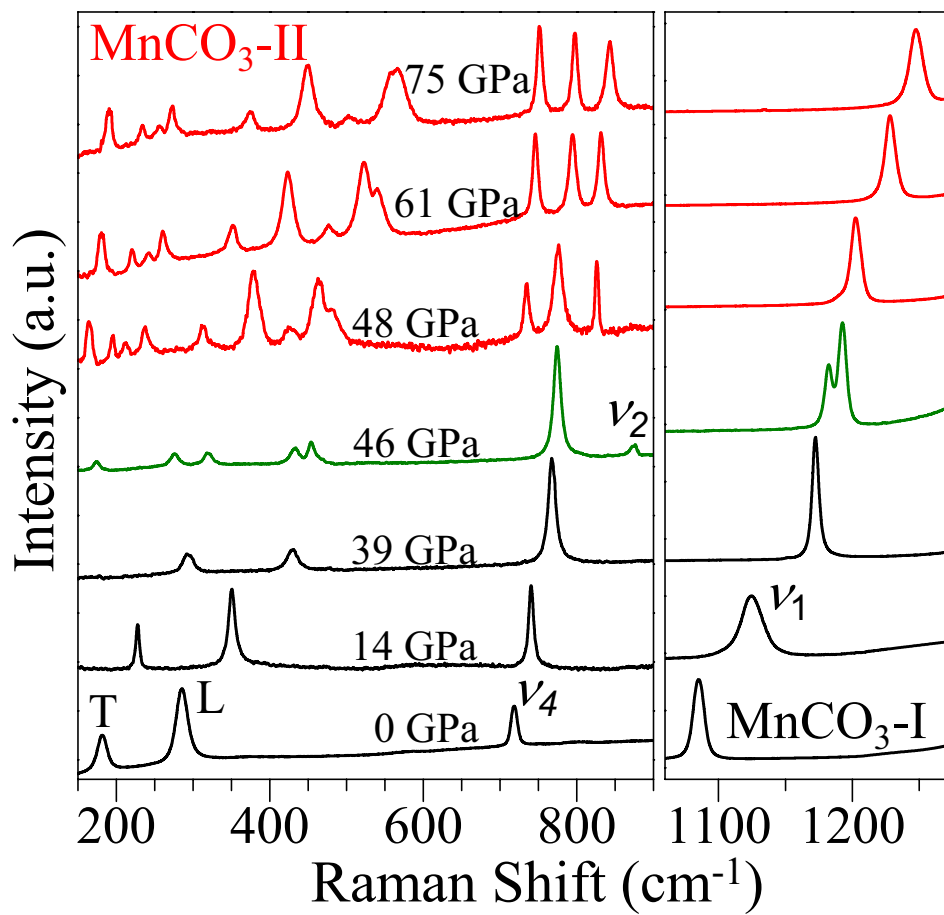
Figure 4

Figure 5

Figure 6

Figure 7

Figure 8

Figure 9